Journal of Chromatography, 484 (1989) 29–59
Elsevier Science Publishers B.V., Amsterdam — Printed in The Netherlands

CHROM. 22 015

MASS TRANSFER EFFECTS IN ISOCRATIC NON-LINEAR ELUTION CHROMATOGRAPHY

CASSIAN K. LEE, QIMING YU, SEUNG UN KIM and NIEN-HWA LINDA WANG*
School of Chemical Engineering, Purdue University, West Lafayette, IN 47907 (U.S.A.)

SUMMARY

In large-scale liquid chromatography, solute competition for sorbent sites (interference) coupled with mass transfer effects can result in complex solute distribution patterns and concentration dependent migration of solute bands. A rate equation model, which accounts for axial dispersion, film mass transfer, intraparticle diffusion, size exclusion and non-linear isotherms, was used to simulate the effluent histories of multicomponent ion-exchange systems. The method of orthogonal collocation on gradient-directed moving finite elements developed by Yu and Wang in 1989 was used to solve the model equations. The theory was verified by comparing the model predictions with data on amino acid and protein ion exchange and good agreement was obtained.

Dimensionless groups were used to identify the local equilibrium regime, in which the effects of axial dispersion, film mass transfer and intraparticle diffusion are negligible. Mass transfer effects were pronounced for systems with small pulse sizes and for solutes with long retention times. For a system with a pulse size about 20 pore volumes $\bar{C}/C_i = 10^3$, and α (separation factor of a solute against eluent) = 1.6, mass transfer effects were negligible at $N_p > 10^3$. For low affinity solutes ($\alpha < 0.1$) of a similar pulse size, local equilibrium was approached at a lower N_p.

The dimensionless groups were also useful for studying the combined effects of design and operating parameters. The effects of these parameters on band shape and band spreading were examined for non-linear systems with various solute affinities. The dimensionless groups were also used to establish simple scaling rules for non-linear chromatography. The scaling rules suggest that one can achieve the same degree of separation but significantly higher throughputs by using small particles, short columns and rapid cycles.

INTRODUCTION

In linear chromatography, solute bands have a simple shape and the mechanisms which cause band spreading during migration in a chromatography column are well understood[1–3]. In non-linear chromatography, however, peak shapes and spreading are affected by solute competition for sorbent sites (interference), axial dispersion, film mass transfer and intraparticle diffusion. As a result, peak shape and spreading are

0021-9673/89/$03.50

complex functions of equilibrium isotherms, mass transfer parameters (film mass transfer coefficients and intraparticle diffusivity), design parameters (particle size and column length), and operating parameters (pulse size, feed concentration and flow-rate). Understanding interference and mass transfer effects on band spreading in non-linear systems is crucial for designing and scaling large-scale chromatography, in which large pulses and concentrated feeds are usually used to increase throughputs.

Because of the complexity of non-linear systems, significant simplifications are usually introduced into chromatography models. In a local equilibrium model, the mass transfer resistances are assumed to be negligible. Therefore, local equilibrium models are useful for explaining thermodynamic effects on the separation and migration of solute bands. They are useful for predicting column dynamics (unsteady state concentration profiles and effluent histories) when mass transfer effects are insignificant. Among them, the interference theory[4–8] provides the most extensive analyses for isocratic systems. However, solutions of local equilibrium models are usually restricted to simple forms of equilibrium isotherms, simple step inputs, and isocratic operations. Only recently, the interference theory was extended to non-linear systems with gradients and two-way flow operations[8]. Also, computer simulations for general non-linear isotherms were carried out recently for isocratic single component gas chromatography (GC) and liquid chromatography (LC)[9], and two-component isocratic LC[10]. Despite the numerous local equilibrium theories, there have been no clear guidelines for judging whether the assumption of local equilibrium is valid for a given system.

For models in the literature that do include mass transfer effects, such as staged models and rate equation models, simplifications are made on equilibrium isotherms or the mass transfer processes. Table I shows a summary of selected theoretical studies that account for mass transfer effects in ion-exchange and adsorption systems. Because of mathematical complexity, detailed solutions are available only for linear isotherm systems, for which interference effect is absent. For non-linear systems, one or more of the following simplifications are used: no intraparticle diffusion, no axial dispersion, no film mass transfer resistance, single component, or special isotherm type. Certain assumptions also make it difficult to study the effects of design and operating parameters. For example, in the linear driving force approach[11], the effects of particle diameter and flow-rate are not explicit. For systems with non-linear isotherms, the lumped mass transfer coefficient estimated under one condition may not apply when solute concentration, particle size, or flow-rate changes. Moreover, a systematic study of axial dispersion, film mass transfer, intraparticle diffusion in non-linear chromatography has not been reported before.

In this article, a detailed rate equation model developed by Yu and Wang[12] is used to study interference and mass transfer effects in non-linear chromatography. The objectives are (1) to verify the rate equation model with experiments on amino acid elution and protein ion exchange; (2) to compare the results with a local equilibrium model in order to identify the regions where the mass transfer effects are negligible; and (3) to study the relative importance of interference, axial dispersion, film mass transfer, and intraparticle diffusion on peak shape and peak spreading under various design and operating conditions.

The model equations expressed in dimensionless form are solved by a gradient-directed moving finite element technique developed by Yu and Wang[12]. Using various

TABLE I

SUMMARY OF RATE EQUATION THEORY LITERATURE

Abbreviations: Adspt = adsorption process; diffusion = intraparticle diffusion; dispersion = axial dispersion; film = film mass transfer; IEX = ion exchange process; LDFA = linear driving force approach.

Ref.	*Feature*	*Isotherm*	*Component*	*Input*	*Method of solution*	*Adspt/ IEX*
24	Diffusion, film	Langmuir	Multi	Batch	Orthogonal collocation	Adspt
25	LDFA	Linear	–	All	Analytical, Laplace transform	Adspt
26	Dispersion, diffusion, film	Linear	–	Step	Analytical, Fast Fourier transform	Adspt
27	Dispersion, diffusion	Parabolic	Single	Step	Finite difference	IEX
28	Diffusion, film	Linear	–	Step	Parabolic & quadratic profiles	Adspt
29	Dispersion LDFA	Langmuir S-shaped	Single	Pulse	Finite difference	Adspt
30	Dispersion, diffusion, film	Linear	–	Pulse	Method of moments	Adspt
31	Dispersion, diffusion, film	Fritz & Schlunder type	Binary	Step	Orthogonal collocation	Adspt
32	Diffusion, film	Linear	–	Step	Parabolic profile	Adspt
33	Diffusion, film, LDFA	Freundlich	Multi	Step	Finite difference	Adspt
34	Dispersion, LDFA	Langmuir	Multi	Step	Finite difference	Adspt
35	Diffusion	Shrinking core	Single	Step	Finite difference	IEX
36	Diffusion	Langmuir	Single	Step	Method of moments	Adspt
37	Diffusion, film	Linear	–	Step	Analytical, Laplace transform	Adspt
38	Two pore diffusion, film	Langmuir	Single	Step	Finite difference	Adspt
39	LDFA	Langmuir, Freundlich	Multi	Step	Finite difference	Adspt
40	Diffusion, film	Langmuir	Single	Step	Numerical	Adspt
41	Dispersion, dual-pore diffusion	Freundlich	Single	Step	Finite difference	Adspt
42	LDFA, non-isothermal	Langmuir	Multi	Step	Method of line	Adspt

dimensionless groups allows us to study the combined effects of design and operating parameters. The magnitudes of these groups indicate the relative importance of film mass transfer, intraparticle diffusion and axial dispersion for a given system. Furthermore, they are useful for scaling of non-linear systems.

THEORY

In formulating this model, we assume uniform packing, uniform velocity distribution, pseudo-homogeneous spherical particles with uniform size distribution, isothermal behavior and constant physical properties. Convection and axial dispersion are considered the only mechanisms of mass transfer in the axial direction. The axial dispersion coefficient is estimated from a standard correlation[13]. The pressure and velocity variations along the axis are assumed to have no effects on equilibrium and column dynamics. The mass transfer coefficient between the bulk mobile phase and the stationary phase is estimated from a J factor correlation[14]. For each particle, its surroundings are assumed to be uniform. Surface diffusion within the particle is also neglected. Along the radial direction in a particle, local equilibrium is assumed between the stagnant fluid in the pores and the sorbent surface.

For each component j, the mass balance equations and initial and boundary conditions are given in eqns. 1 and 2, where subscripts b and p denote the bulk and particle phases, respectively.

Bulk phase

$$\frac{\partial c_{bj}}{\partial \tau} = \frac{1}{Pe_z}\frac{\partial^2 c_{bj}}{\partial x^2} - \frac{\partial c_{bj}}{\partial x} - N_{bj}(c_{bj} - c_{pj,\xi=1}) \tag{1a}$$

$$x = 0, \quad \frac{\partial c_{bj}}{\partial x} = Pe_z(c_{bj} - c_{fj}) \tag{1b}$$

$$x = 1, \quad \frac{\partial c_{bj}}{\partial x} = 0 \tag{1c}$$

$$\tau = 0, \quad c_{bj} = c_{bj}(0,x) \tag{1d}$$

where

$$\tau = t/(L/u_0), \quad x = z/L, \quad N_{bj} = \frac{L}{R}\frac{3(1-\varepsilon)}{\varepsilon}\frac{Bi_j}{Pe_{pj}}, \quad Bi_j = k_j R/E_{pj},$$
$$Pe_z = u_0 L/E_{bj}, \quad Pe_{pj} = u_o R/E_{pj}.$$

All concentration variables are normalized by their respective feed concentrations. Thus, c_{bj} is a dimensionless bulk phase concentration, c_{fj} is a dimensionless feed concentration, z is the axial distance, L is the column length, R is the particle radius, t is time, u_0 is the interstitial velocity, k_j is the film mass transfer coefficient of component

j, ε is the bed void fraction and E_{bj} and E_{pj} are the axial dispersion coefficient and effective diffusivity of component j, respectively.

Particle phase

$$Ke_j\left[\theta\frac{\partial c_{pj}}{\partial\tau}+(1-\theta)\frac{\partial c^*_{pj}}{\partial\tau}\right]=N_{pj}\frac{1}{\xi^2}\frac{\partial}{\partial\xi}\left[\xi^2\frac{\partial c_{pj}}{\partial\xi}\right] \tag{2a}$$

$$\xi=0,\quad \frac{\partial c_{pj}}{\partial\xi}=0 \tag{2b}$$

$$\xi=1,\quad \frac{\partial c_{pj}}{\partial\xi}=Bi\,(c_{bj}-c_{pj}) \tag{2c}$$

$$\tau=0,\quad c_{pj}=c_{pj}(0,\xi) \tag{2d}$$

where $\xi=r/R$, $N_{pj}=(L/R)\cdot(1/Pe_{pj})$, c_{pj} is the local dimensionless concentration of component j in the fluid phase within a particle, c^*_{pj} is the dimensionless concentration of component j in the solid phase within a particle and it is in equilibrium with the local concentrations of the fluid phase ($c_{p1}, c_{p2}, \ldots, c_{pn}$), n is the number of components, r is the radial coordinate of the particle, θ is intraparticle porosity, and Ke_j is the size exclusion factor of component j.

One of the objectives of this study is to compare the results of the rate equation model with those from a previous local equilibrium model based on the assumption of constant separation factors[7]. The comparison is needed to identify the conditions under which the local equilibrium model is applicable. For this reason, the equilibrium isotherms here are represented by constant separation factors. For a multicomponent system with constant separation factors, the non-linear equilibrium isotherm for component i can be written as follows

$$c^*_{pi}=\frac{c_i\bar{C}/C_i}{\alpha_{1i}\sum_j\frac{c_j}{\alpha_{1j}}} \tag{3}$$

where α_{ij} is the separation factor of i against j, $\bar{C}$ is column capacity per bed volume, C_i is the feed concentration of the i^{th} component based on per bed volume, and $\bar{C}/C_i$ is an important dimensionless group. Although all simulations reported in this paper are for constant separation factor systems, this model can incorporate any complex isotherms. Simulations for systems with Langmuir isotherms have been reported in a previous paper[12].

The dimensionless group Pe_z in eqn. 1 is the axial Peclet number, which is proportional to the ratio of a characteristic convection rate to that of axial dispersion. The dimensionless group Pe_p in eqn. 2 is the particle Peclet number, which is proportional to the ratio of a characteristic convection rate to that of intraparticle diffusion. The Biot number (Bi) in eqn. 2 represents the ratio of a characteristic film mass transfer rate to that of intraparticle diffusion.

A correlation developed by Chung and Wen[13] is used to estimate E_b or Pe_z.

$$Pe_z = \frac{L}{2R\varepsilon}(0.2 + 0.011Re^{0.48}) \tag{4}$$

where the Reynolds number (Re) is defined as

$$Re = \frac{2R\rho u_0 \varepsilon}{\mu} \tag{5}$$

Since Re is typically in the order of 0.1 or less, Pe_z is essentially only a function of $L/(R\varepsilon)$.

The film mass transfer coefficient k can be estimated from a J factor correlation proposed by Wilson and Geankoplis[14]. This correlation is valid for liquid systems with low Reynolds numbers.

$$J = \left(\frac{k}{u_0\varepsilon}\right)\left(\frac{\mu}{\rho D^\infty}\right)^{2/3} = \frac{1.09}{\varepsilon} Re^{-2/3} \tag{6}$$

As shown in eqn. 6, the film mass transfer coefficient k is related to D^∞ (Brownian diffusivity) and u_0 (interstitial velocity). The effective intraparticle diffusivity (E_p) of a solute is also related to D^∞ for a given sorbent material (see eqn. 10). Because of this interdependence, one can rearrange eqn. 6 to give the following explicit relation:

$$\frac{u_0}{k} = \left[\frac{(2\varepsilon)^{2/3}}{1.09}\right]\left(\frac{E_p}{D^\infty}\right)^{2/3}\left(\frac{Ru_0}{E_p}\right)^{2/3} \tag{7}$$

which is equivalent to

$$Pe_p/Bi = \left[\frac{(2\varepsilon)^{2/3}}{1.09}\right]\left(\frac{E_p}{D^\infty}\right)^{2/3}(Pe_p)^{2/3} \tag{8a}$$

or

$$Pe_p = \left[\frac{(1.09)^{3/2}}{2\varepsilon}\right]\left(\frac{D^\infty}{E_p}\right)\left(\frac{Pe_p}{Bi}\right)^{3/2} \tag{8b}$$

Eqn. 8b can be rearranged to give an explicit relation between Pe_p and Bi.

$$Pe_p = \frac{4\varepsilon^2}{1.09^3}\left(\frac{E_p}{D^\infty}\right)^2 Bi^3 \tag{9}$$

Eqn. 9 suggests that as Pe_p increases with increasing particle size or flow-rate, Bi also increases. This implies that as Pe_p increases, intraparticle diffusion resistance becomes relatively more important than film resistance.

We are interested in comparing simulation results with data for amino acid and protein ion exchange here, but unfortunately, experimental data of E_p are usually unavailable. For small ions and particles with uniform pores, the following equation can be applied to estimate E_p from Brownian diffusivity D^{∞}[15,16].

$$E_p = \left(\frac{\theta}{2-\theta}\right)^2 D^{\infty} \tag{10}$$

If this equation is used, eqn. 9 becomes

$$Pe_p = \frac{4\varepsilon^2}{1.09^3}\left(\frac{\theta}{2-\theta}\right)^4 Bi^3 \tag{11}$$

Pulse size is another important scaling parameter for this system. A dimensionless pulse size $\Delta\tau$ is defined here as

$$\Delta\tau = \frac{V_p}{\varepsilon V_{bed}} = \frac{V_p u_0}{FL} \tag{12}$$

where F is volumetric flow-rate, V_p is the volume of a feed pulse and V_{bed} is bed volume. As shown in eqn. 12, $\Delta\tau$ represents a dimensionless pulse volume, where V_p is normalized by interparticle void volume (εV_{bed}) in a packed bed. This dimensionless pulse $\Delta\tau$ is related to the fractional loading ΔT_i, which was defined previously for local equilibrium studies[4,8].

$$\Delta T_i = \frac{C_i \Delta\tau}{\bar{C}} \tag{13}$$

This fractional loading also represents a dimensionless pulse size, in which the total amount of solute i input to the column during $\Delta\tau$ is normalized by total column capacity.

Eqn. 9 (or eqn. 11) can be substituted into eqns. 1 and 2 to eliminate Pe_p. Thus, we are left with Pe_z and Bi as the independent transport parameters, L/R, ε and θ (and E_p/D^{∞}, if eqn. 10 is used) are the system parameters, $\bar{C}/C_i$ and $\Delta\tau$ are the operating parameters. These dimensionless parameters are useful for scaling purposes and for studying the combined effects of L, R and u_0. They are especially convenient for estimating the relative importance of intraparticle diffusion, film mass transfer, and axial dispersion on band spreading for a given system. These results will be discussed later.

Since the systems being studied involve non-linear isotherms, eqns. 1 and 2 must be solved numerically. An efficient numerical method was developed by Yu and Wang[12] for solving non-linear boundary value problems. This method, being

especially useful for fixed-bed systems with steep gradients, was used to solve the model equations here. It employs orthogonal collocation on both bulk and particle phases as well as a gradient-directed moving finite elements scheme. Details of this technique and convergence behavior are available elsewhere[12]. A typical elution simulation requires two collocation points in the particle phase and four points in each element for the bulk phase. The number of elements varies from 16 initially to about 4 at the end of simulation.

RESULTS AND DISCUSSION

Before studying mass transfer effects and interference phenomena, we verified this model with data from ion exchange of amino acids and proteins. Previous data on isocratic elution of lysine and proline were considered first[17]. A 7.5 × 1 cm I.D. column was used. It was packed with Bio-Rad AG 50W-X8 cation-exchange resin, with a particle radius of about 25 μm. A 50-ml mixture of 0.01 N lysine and 0.01 N proline in 0.19 N of sodium citrate buffer at pH 4.4 was injected into the column at 2 ml/min, and eluted with 0.20 N of sodium citrate buffer at the same pH. Fig. 1a shows the effluent history of the column plotted in dimensionless concentration *versus* dimensionless time. The results from the rate equation model (solid lines) are compared with those from the local equilibrium model (dashed lines). As the figure shows, the local equilibrium model can predict the average retention time, but it cannot predict the exact product concentration and zone spreading behavior because it neglects mass transfer effects.

As mentioned before, both axial dispersion and film diffusion coefficients were estimated from standard correlations. Since E_p values were not readily available for this sytem, approximate values were obtained from eqn. 10. Except where indicated, eqn. 10 was used to estimate E_p from D^∞ for all simulations in this paper. An E_p of 3.5 $\cdot 10^{-5}$ cm^2/min was used for both lysine and proline for the simulations shown in Fig.

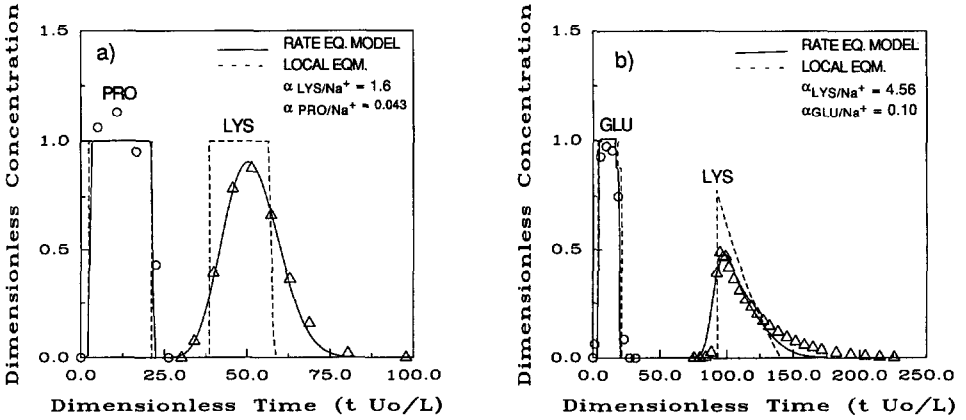

Fig. 1. (a) Experimental results and model predictions of the lysine–proline system. $Pe_z = 672$, $Pe_p = 337$, $Bi = 42$, $Pe_p/Bi = 8$, $\Delta\tau = 18.86$, $\alpha_{Lys/Na^+} = 1.6$, $\alpha_{Pro/Na^+} = 0.043$. Parameters used in simulations are listed in Table II. (b) Experimental results and model predictions of the lysine–glutamic acid system. $Pe_z = 653$, $Pe_p = 202$, $Bi = 36$, $Pe_p/Bi = 5.6$, $\Delta\tau = 15.50$, $\alpha_{Lys/Na^+} = 4.56$, $\alpha_{Glu/Na^+} = 0.10$.

1a. The value of D^{∞} was first estimated from the Wilke–Change correlation given in ref. 18 and eqn. 10 was then used to estimate E_p. This E_p value is similar to the values given for other amino acids in a similar exchanger[19]. The same separation factors from the local equilibrium simulation were used ($\alpha_{Lys/Na^+} = 1.6$ and $\alpha_{Pro/Na^+} = 0.043$). Both bed void fraction (ε) and particle porosity (θ) were 0.45. All the parameter values used for simulations are listed in Table II.

Because proline has a low affinity relative to Na^+, it elutes immediately without any peak broadening, and the concentration is the same as in the feed pulse. This behavior is closely predicted by both models. For the lysine peak, only the rate equation model can predict the experimental behavior in detail. Because the retention time of lysine is longer and mass transfer effects are more pronounced, the lysine peak becomes less concentrated than the feed and it spreads more than the proline peak. This example shows the validity and accuracy of the rate model for high affinity solutes.

Fig. 1b shows the results of elution of a glutamic acid and lysine mixture. A 7.3-cm column packed with the same resin was used, and a pulse of 40 ml with 0.02 *N* lysine, 0.01 *N* glutamic acid and 0.20 *N* sodium citrate was injected into the column at a flow-rate of 1 ml/min. It was then eluted with 0.20 *N* of sodium citrate buffer at pH 3.5[8]. At this pH, α_{Glu/Na^+} is 0.10, and α_{Lys/Na^+} is 4.56, which is much higher than in the previous case. The rate equation model again can predict the data closely by using the same E_p, θ and ε as in the previous system. For the same reason as in the previous case,

TABLE II

SUMMARY OF PARAMETER VALUES USED FOR SIMULATIONS

$\theta = \varepsilon = 0.45$, $E_p = 4.2 \cdot 10^{-5}$ cm²/min, $D^{\infty} = 5 \cdot 10^{-4}$ cm²/min, $\bar{C} = 2.3$ mequiv./ml packed volume.

Fig.	*L (cm)*	*V_p (ml)*	*F (ml/min)*	*R (μm)*	α_{Lys/Na^+}	α_{Pro/Na^+}	*[Lysine] (N)*	*[Proline] (N)*	*[Na^+] (N)*
1a[a]	7.5	50	2	25	1.6	0.043	0.01	0.01	0.19
1b[a]	7.3	40	1	25	4.56	0.10[b]	0.02	0.01[b]	0.20
4	7.5	50	0.1–40	25	1.6	0.043	0.01	0.01	0.18
7	7.5	50	0.5–40	25	4.0	0.5	0.01	0.01	0.18
8–10					1.6	0.043	0.01	0.01	0.18
13a	7.5	50	2	25–160	1.6	0.043	0.01	0.01	0.18
13b	7.5	50	2	10–100	4.0	0.5	0.01	0.01	0.18
14	1–15	50	2	25	1.6	0.043	0.01	0.01	0.18
15	7.5	10–250	2	25	1.6	0.043	0.01	0.01	0.18
16a	7.5	50	2	25	1.6	0.043	0.01–0.16	0.01–0.16	0.18
16b[c] (1)	7.5	50	2	25	1.6	0.043	0.01	0.01	0.18
(2)							0.031	0.031	0.139
(3)							0.047	0.047	0.106
(4)							0.064	0.064	0.072
16c	7.5	100	2	25	1.6	0.043	0.01–0.16	0.01–0.16	0.18
17a	7.5	100	2	25	1.6	0.043	0.04	0.04	0.04–0.34
17b	7.5	50	2	25	1.6	0.043	0.04	0.04	0.04–0.34

[a] $E_p = 3.5 \cdot 10^{-5}$ cm²/min, $D^{\infty} = 4.16 \cdot 10^{-4}$ cm²/min.

[b] $\alpha_{Glu/Na^+} = 0.10$, $c_{Glu} = 0.01$ *N*.

[c] The fractions of lysine, proline and Na^+ are the same as in Fig. 16a except the total concentration is kept at 0.2 *N*.

the glutamic acid passes through the column immediately without any zone spreading. For this low affinity solute, because mass transfer effects are insignificant, the local equilibrium model is adequate. Asymmetric lysine peak is predicted by both models. This is because solute migration speed is a function of solute concentration and α; the larger the α or the higher the solute concentration, the more does the migration speed vary with concentration, and the more pronounced is the tailing[8]. Again in this case, the rate equation model is needed to predict the lysine data accurately.

Experimental data obtained from protein ion exchange were also used to verify the model. An 11-cm column packed with DEAE Sepharose Fast Flow (Pharmacia) was presaturated with chloride ions initially. A 5-mg/ml myoglobin (Myo) solution in 0.1 *M* Tris buffer at pH 8 was injected into the column at a flow-rate of 0.5 ml/min. Bovine serum albumin (BSA) with the same concentration as myoglobin was introduced into the column to displace myoglobin after 111 min ($\tau = 18.36$). The effluent history is shown in Fig. 2a. Because of the size of protein molecules, not the whole resin particle is accessible to the protein; therefore, size-exclusion factors of 0.72 and 0.6 (ref. 8) were used for myoglobin and BSA, respectively, to obtain the simulation results in Fig. 2a.

The E_p values for the proteins were estimated from the Brownian diffusivities using eqn. 10 ($\theta = 0.95$). They were $5.55 \cdot 10^{-5}$ cm^2/min for myoglobin[20], $3.34 \cdot 10^{-5}$ cm^2/min for BSA[21] and $9.98 \cdot 10^{-4}$ for Cl^- (ref. 18). Values of $\alpha_{BSA/Cl^-} = 6.0$ and $\alpha_{Myo/Cl^-} = 1.5$ were used to obtain the curves in Fig. 2a. As the figure shows, this rate equation model gives close prediction for this system. It appears that under the experimental conditions, ion exchange of both BSA and myoglobin is reversible. If the proteins undergo slow adsorption or desorption, this model is not expected to give good predictions.

For the same system except with 20 mg/ml each of BSA and myoglobin, 5.5 cm column length and 0.25 ml/min flow-rate, the effluent history is shown in Fig. 2b. In this case, BSA was introduced after 102 min ($\tau = 16.87$) to displace myoglobin. The same size-exclusion factors, separation factors and diffusion coefficients used in Fig. 2a were used to obtain the result here. Again, the model predicts closely the experimental data.

The results from a local equilibrium model are also included in Fig. 2a and b for comparison. Identical parameters as in the rate model were used. The definition of adjusted time T reported previously was modified here in order to take into account intraparticle porosity θ and size exclusion.

$$T_j = \frac{Cu_0}{Ke_j\bar{C}L}\left\{ t - \frac{L}{u_0}\left[1 + \frac{(1 - \varepsilon)Ke_j\theta}{\varepsilon}\right]\right\} \tag{14}$$

For the cases with multiple step changes (Fig. 2a and b), the local equilibrium model gives good predictions of the average breakthrough times, but not the details of the breakthrough curves.

Mass transfer analysis by dimensionless groups

The dimensionless groups defined in this paper (Pe_z, Pe_p, Bi, L/R, $\bar{C}/C_i$ and $\Delta\tau$) are important scaling parameters. They are also helpful for identifying the local

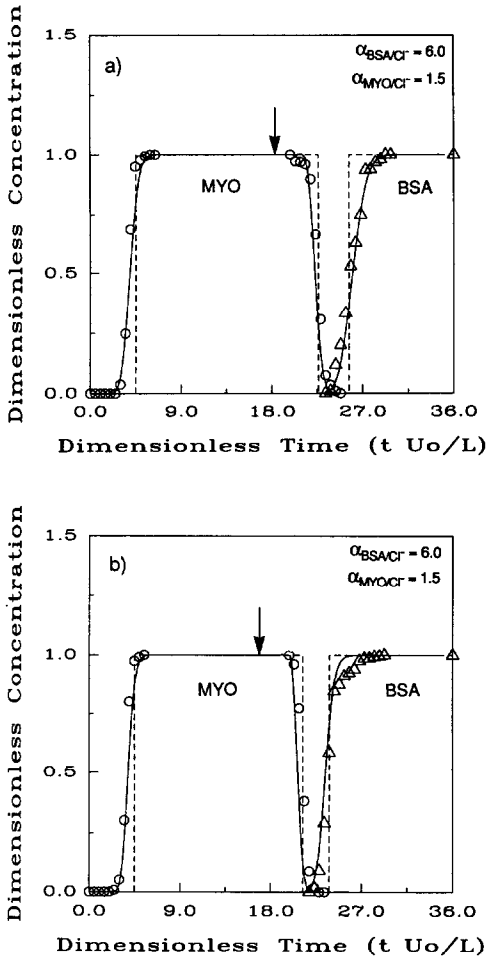

Fig. 2. (a) Experimental results and model predictions of the BSA–myoglobin system. Pe_z = 632, $Pe_{p,Myo}$ = 164, $Pe_{p,BSA}$ = 272, Pe_{p,Cl^-} = 9.11, Bi_{Myo} = 8.65, Bi_{BSA} = 10.24, Bi_{Cl^-} = 3.30. L = 11.0 cm, R = 50 μm, F = 0.5 ml/min, c_{BSA} = c_{Myo} = 5 mg/ml, c_{Cl^-} = 0.16 N. (b) Experimental results and model predictions of the BSA–myoglobin system. Pe_z = 316, $Pe_{p,Myo}$ = 81.9, $Pe_{p,BSA}$ = 136, Pe_{p,Cl^-} = 4.56, Bi_{Myo} = 6.86, Bi_{BSA} = 8.13, Bi_{Cl^-} = 2.62. L = 5.5 cm, R = 50 μm, F = 0.25 ml/min, c_{BSA} = c_{Myo} = 20 mg/ml, c_{Cl^-} = 0.16 N. Solid lines represent the predictions of the rate equation model; dashed lines represent predictions of the local equilibrium model; and arrows indicate the times of step input of BSA solution.

equilibrium regime and for understanding the relative importance of film mass transfer, intraparticle diffusion and axial dispersion for a given system.

Local equilibrium region. Since *Bi* gives the ratio of intraparticle diffusion resistance over film mass transfer resistance, the absolute magnitude of the two resistances are not clear from this parameter. In order to identify the region that has negligible mass transfer resistances (local equilibrium conditions), other dimensionless groups must be examined. The N_{bj} parameter in the film mass transfer term of eqn. 1a, which consists of L, R, ε, Pe_p and Bi, can be taken as a normalized film mass transfer

rate. The N_{pj} of eqn. 2a can be taken as a normalized intraparticle diffusion rate. For a given system, a plot of $1/N_{pj}$ against $1/N_{bj}$ shows how normalized intraparticle diffusion resistance changes with normalized film resistance (Fig. 3). At the lower left corner of the plot, both intraparticle diffusion and film resistances are negligible. If $1/Pe_z$ is plotted as the third axis, then the origin is the true local equilibrium point.

Eqn. 8b can be modified to give the following relationship between N_p and N_b.

$$N_p = \left(\frac{3(1-\varepsilon)}{\varepsilon}\right)^{3/2} \left(\frac{L}{R}\right)^{1/2} \left(\frac{1.09^{3/2}}{2\varepsilon}\right) \left(\frac{D^\infty}{E_p}\right) N_b^{3/2}$$

This implies that for a given set of ε, L/R, D^∞/E_p (or θ, if eqn. 10 is valid), all possible $1/N_p$ and $1/N_b$ values form a straight line with a slope of 1.5 in a log–log plot (Fig. 3). For example, at $\theta = \varepsilon = 0.45$, $\Delta\tau = 18.86$ and $L/R = 3000$, the seven triangle points represent the cases with seven different flow-rates shown in Fig. 4 (see Table II for values of other parameters) and indeed, they follow a straight line. It should be noted that Pe_z is the third parameter, and these seven points have slightly different Pe_z.

As the flow-rate decreases, both $1/N_p$ and $1/N_b$ decrease along the line. It has been found that there are no changes in the effluent history when the flow-rate is less than 0.1ml/min. Therefore, the elution peaks approach a limiting shape, which occurs at about $Bi = 16$ and $Pe_p = 17$. In order to approach local equilibrium conditions at this point, L/R needs to be increased to further reduce $1/N_b$ and $1/N_p$. Fig. 5 shows the results at various L/R values while all other dimensionless parameters are kept constant. Since $\Delta\tau$ (= 18.86) is fixed, increasing L requires increasing V_p in these cases. As L/R increases to 12000, the peak of high-affinity solute approaches the local equilibrium curve at $N_p = 7.1 \cdot 10^2$, $N_b = 4.1 \cdot 10^4$ and $Pe_z = 2.7 \cdot 10^3$.

When $\Delta\tau$ was decreased to 0.377 with all other parameters kept the same as in

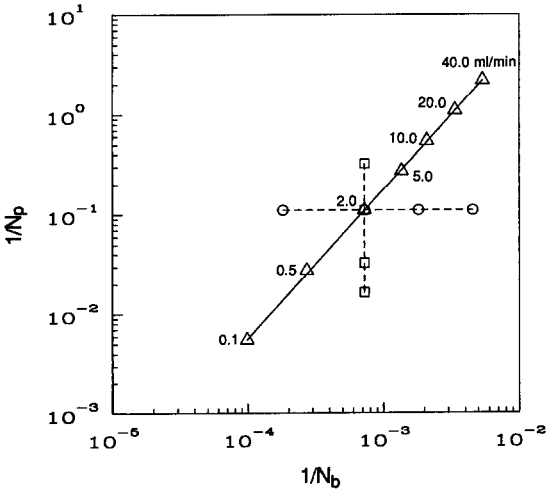

Fig. 3. Normalized intraparticle diffusion resistance ($1/N_p$) *versus* normalized film resistance ($1/N_b$). The same parameters as those in Fig. 1a except different flow-rates are used in calculating the seven triangles. The four circles represent the four cases shown in Fig. 9. The four squares represent the four cases shown in Fig. 10.

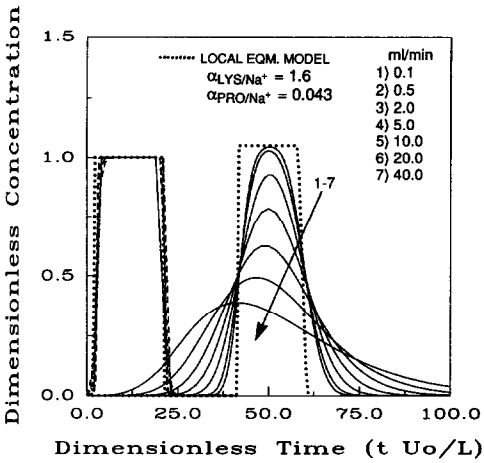

Fig. 4. Effect of flow-rate. Parameters correspond to the seven triangles in Fig. 3. Lysine and proline histories predicted from the rate equation model are shown in solid lines and dashed lines, respectively. Predictions from the local equilibrium model are shown in dotted lines.

Fig. 4, the effluent histories of the highly retained solute at four different flow-rates are shown in Fig. 6. Note the heights of the peaks are less than 0.05 in dimensionless concentration. At flow-rates below 0.01 ml/min, no changes were observed. Actually, the 0.1 ml/min curve is already very close to the limiting shape.

Attempts were made to increase L/R (to further decrease $1/N_b$ and $1/N_p$) to approach local equilibrium conditions. The dashed curves shown in Fig. 6 were simulated at 0.01 ml/min flow-rate, and L/R = 15 000 (Pe_z = 3340) and L/R = 60 000 (Pe_z = 13 360). The peaks do become sharper, but they are still very far from reaching 1.0 (where the local equilibrium peak would reach). Further increase of L/R (and also Pe_z) would require substantially longer computation time because of numerical

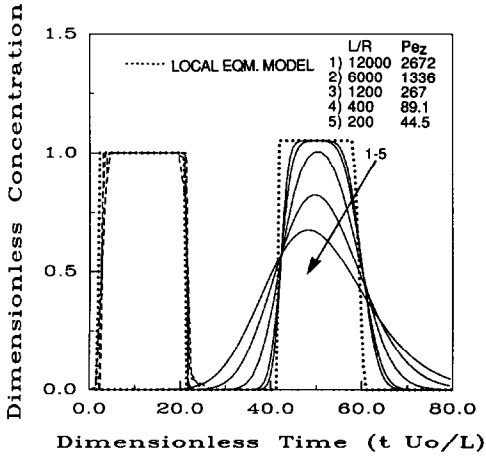

Fig. 5. Varying L/R for the case at 0.1 ml/min flow-rate in Fig. 4.

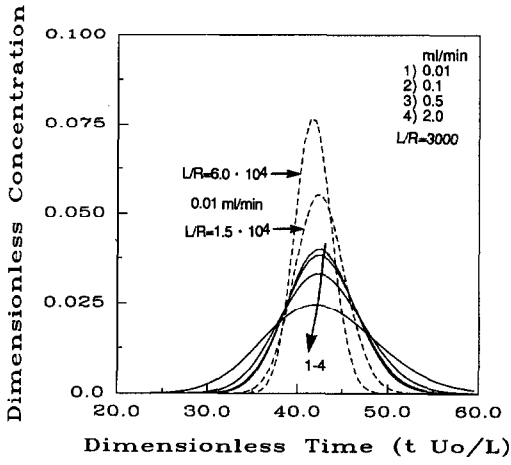

Fig. 6. Approaching local equilibrium conditions with $\Delta\tau = 0.377$. Unless noted otherwise, all the other parameters are the same as those for Fig. 5.

difficulties. This result shows that for a smaller $\Delta\tau$, it requires larger values of N_b and N_p to approach local equilibrium.

The affinity of the solute (α) is another factor that affects the region of local equilibrium. Fig. 7 shows the results for $\Delta\tau = 18.86$ but with a different set of α values ($\alpha_{Lys/Na+} = 4.0$ and $\alpha_{Pro/Na+} = 0.5$ in Fig. 7, compared to $\alpha_{Lys/Na+} = 1.6$ and $\alpha_{Pro/Na+} = 0.043$ in Fig. 4). All other parameters in these two figures are identical. For the solute with $\alpha = 0.043$ (Fig. 4), the peak at 40 ml/min flow-rate ($N_p \approx 0.5$) is very similar to the local equilibrium peak. For the solute with $\alpha = 0.5$ (Fig. 7), local equilibrium is approached at 0.5 ml/min ($N_p = 35.6$, $N_b = 3.5 \cdot 10^3$ and $Pe_z = 670$).

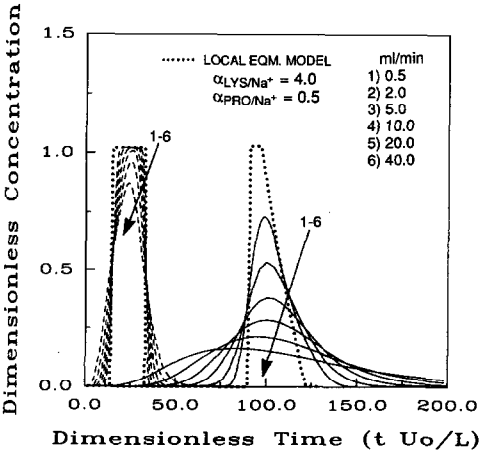

Fig. 7. Effect of flow-rate. The parameters are the same as those in Figs. 1a and 4 except $\alpha_{Lys/Na+} = 4.0$ and $\alpha_{Pro/Na+} = 0.5$.

For the solute with $\alpha = 1.6$ (Fig. 4), local equilibrium is approached at 0.1 ml/min ($N_p = 7.1 \cdot 10^2$, $N_b = 4.1 \cdot 10^4$ and $Pe_z = 2.7 \cdot 10^3$). For the solute with $\alpha = 4$ (Fig. 7), even the peak at the lowest flow-rate is still quite different from that at local equilibrium. Therefore, the larger the α, the larger the values of N_p, N_b and Pe_z required to approach local equilibrium.

Effect of Pe_z. Changing E_b changes only Pe_z, and all other parameters remain constant. This way, the isolated effect of the Pe_z term in eqn. 1a can be studied. Fig. 8a shows the effluent history of the same lysine–proline system discussed earlier. Assuming that Pe_z can be varied independently, one can plot the results for Pe_z at 1000, 500, 200, 100, 50 and 5. The other parameters are $Pe_p = 100$, $Bi = 28$, $\varepsilon = \theta = 0.45$ and $L/R = 3000$. The lysine peak ($\alpha = 1.6$) at $Pe_z = 500$ is very close to that at $Pe_z = 1000$, but it is still quite different from that at $Pe_z = 200$. Therefore, a Pe_z of 1000 is the limit for negligible axial dispersion for lysine. Axial dispersion broadens the bands and

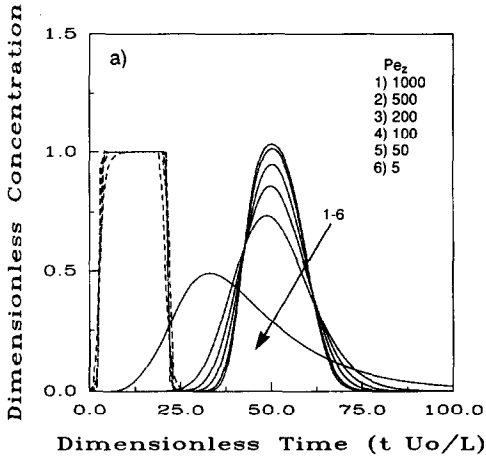

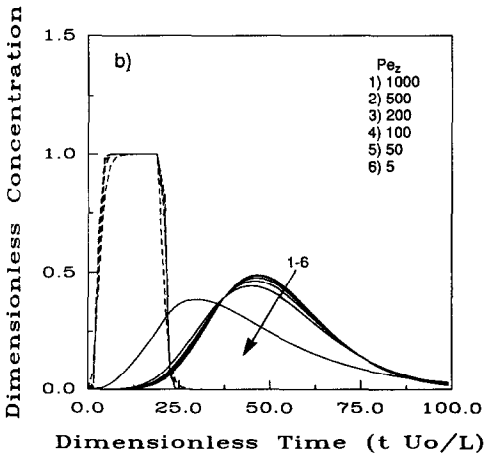

Fig. 8. (a) Effect of axial dispersion at $Pe_p = 100$, $Bi = 28.2$, $L/R = 3000$, $\Delta\tau = 18.86$. (b) Effect of axial dispersion at $Pe_p = 3370$, $Bi = 91.2$, $L/R = 3000$, $\Delta\tau = 18.86$.

eventually produces asymmetric peaks at small Pe_z. For the proline peak ($\alpha = 0.043$), axial dispersion and film and intraparticle diffusion have negligible effects on band spreading.

The effects of axial dispersion are relatively more pronounced when Pe_p and Pe_p/Bi are small (close to local equilibrium conditions). When intraparticle resistance or film resistance is large, axial dispersion has very minor effects. For example, for the same system shown in Fig. 8a except at $Pe_p = 3370$ and $Bi = 91.2$, the results for the same set of Pe_z numbers are shown in Fig. 8b. In this case, the lysine peak is broadened by large intraparticle diffusion resistance. Changing Pe_z from 1000 to 100 has almost no effect, and minor effect for $Pe_z = 50$. At $Pe_z = 5$, the lysine peak becomes noticeably more asymmetric and overlaps with the proline peak. Therefore for $Pe_p = 3370$ and $Bi = 91.2$, the limit for negligible axial dispersion is around Pe_z of 50, which is considerably smaller than the limit in Fig. 8a.

Effects of Pe_p/Bi and Pe_p. It is also worthwhile to study the isolated effects of the film mass transfer term (Pe_p/Bi) in eqn. 1a and intraparticle effective diffusion term (Pe_p) in eqn. 2a. Fig. 9 shows the results when keeping all dimensionless parameters constant and changing only k to vary Pe_p/Bi. The four curves shown here are represented by the four circles in Fig. 3: $Pe_p = 337$, $L/R = 3000$ and Pe_p/Bi ranging from 2 to 50. This gives Bi ranging from 169 to 6.7. As k decreases, Bi decreases, and the lysine peak ($\alpha = 1.6$) becomes broader and less concentrated, but relatively small changes are observed in this range of Bi. For the same reason mentioned before, because the low affinity of the proline peak ($\alpha = 0.043$), changing k or Pe_p/Bi has no effects at all. Moreover, as k increases (or Pe_p/Bi decreases), a limiting peak shape indicates negligible film resistance.

Fig. 10 shows the results when keeping $Pe/Bi = 8$, $L/R = 3000$ and changing Pe_p from 50 to 1000. This provides the effect of changing E_p (or Pe_p) alone. The four curves are also represented as squares in Fig. 3. As E_p decreases, both Pe_p and Bi increase. This leads to broadening of the lysine peak. A limiting peak shape is expected for large E_p values which correspond to negligible intraparticle diffusion resistance.

The results shown in Figs. 8–10 indicate that for the experimental systems tested,

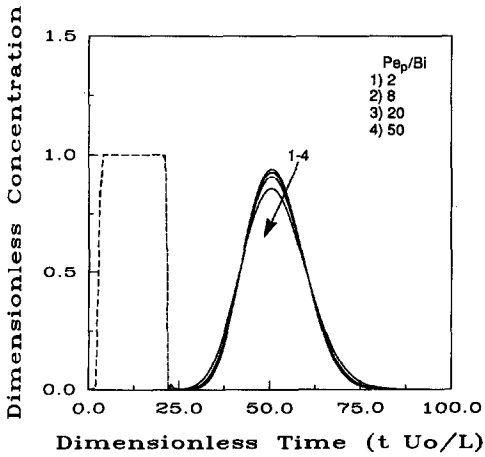

Fig. 9. Effect of Pe_p/Bi at $Pe_z = 672$, $Pe_p = 337$, $L/R = 3000$, $\Delta\tau = 18.86$.

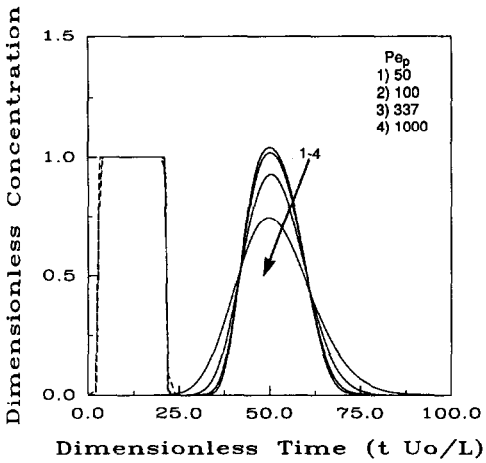

Fig. 10. Effect of Pe_p at $Pe_z = 782$, $Pe_p/Bi = 8$, $L/R = 3000$, $\Delta\tau = 18.86$.

axial dispersion and film resistance are unimportant; intraparticle diffusion resistance is the major cause for lysine band spreading (Fig. 1a and b) and the spreading of BSA and myoglobin breakthrough curves (Fig. 2a and b). Therefore, the good agreement between data and model predictions shown in Figs. 1 and 2 does not prove the accuracy of the correlations for axial disperision coefficient (eqn. 4) and film mass transfer coefficient (eqn. 6). Thorough testing of these correlations and others[22] requires further studies of systems for which axial dispersion and film resistance are dominating.

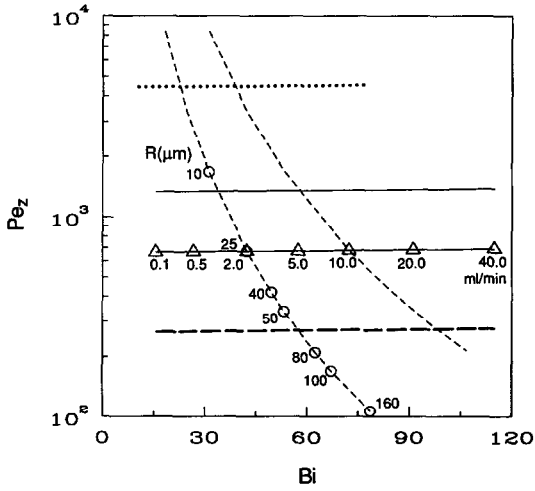

Fig. 11. *Pe_z versus Bi* at various operating conditions. The seven triangles from Fig. 3 are shown here. ---○---: R varies from 2 to 160 μm, while all other parameters are the same as those for the case with 2 ml/min flow-rate. ------: R varies from 2 to 160 μm, while all other parameters are the same as those for the case with 10 ml/min flow-rate. ———: $R = 25$ μm, $L = 15$ cm, flow-rate varies from 0.1 to 40 ml/min. – – – –: $R = 25$ μm, $L = 3$ cm, flow-rate varies from 0.1 to 40 ml/min. ·····: $R = 7.5$ μm, $L = 15$ cm, flow-rate varies from 0.1 to 40 ml/min.

Variation of dimensionless parameters with operating parameters. Since Pe_p is related to *Bi*, a plot of Pe_z *vs. Bi* would be sufficient to represent an entire fixed-bed system for a given set of L/R, $\Delta\tau$, $\bar{C}/C_i$, ε and θ (or E_p/D^∞). Fig. 11 shows the ranges of Pe_z and *Bi* that are encompassed by some typical operating conditions for a column of 1 cm I.D. The triangles shown in Fig. 3 are plotted here. These data are from a 7.5 cm × 1 cm I.D. column with 25-μm particles at different flow-rates (effects of flow-rate are shown in Fig. 4 and will be discussed later).

From the *J* factor correlation discussed earlier, the film mass transfer coefficient k increases with $u_0^{1/3}$. Because the normalized film resistance $1/N_b$ is proportional to u_0/k, it increases with $u_0^{2/3}$. The normalized intraparticle diffusion resistance $1/N_p$ increases linearly with u_0. As a result, as flow-rate increases, *Bi* increases and intraparticle diffusion resistance becomes more important relative to film resistance. The axial Peclet number Pe_z, on the other hand, has a very weak dependence on flow-rate because *Re* is typically 0.1 or less (see eqn. 4). As shown in Fig. 11, *Bi* ranges from 15.6 for 0.1 ml/min to 115 for 40 ml/min, while Pe_z only varies from 665 to 692. The ratio L/R has a major effect on Pe_z. When column length is increased from 7.5 cm to 15 cm, Pe_z increases proportionally (see solid line above). Pe_z values range from 1340 (0.1 ml/min) to 1385 (40 ml/min). On the other hand, when column length is decreased to 3 cm, Pe_z becomes much lower, ranging from 265 to 277 (see dashed line below).

The dotted line shown on the top of Fig. 11 is from a 15-cm column with 7.5 μm particle radius at different flow-rates. The flow-rate range is the same as the previous cases but for this smaller particle radius and longer column, the *Bi* ranges from 10.4 to 77 instead of 15.6 to 115 for $R = 25$ μm.

The circles in Fig. 11 are values for a 7.5-cm column at a flow-rate of 2 ml/min and different particle radii (which will be discussed later). It ranges from $Pe_z = 1676$ and $Bi = 31.2$ ($R = 10$ μm) to $Pe_z = 107$ and $Bi = 78.6$ ($R = 160$ μm). The dashed curve joining the circles is extended to $R = 2$ μm at a Pe_z over 8000. Therefore, increasing particle size not only decreases Pe_z, it also increases *Bi* at the same time.

When the flow-rate is increased from 2 ml/min to 10 ml/min, the whole curve for 2 ml/min just shifts to the right. It should be noticed that when these two curves intersect the varying flow-rate lines, it means two different sets of flow-rate, column length and particle size would give the same Pe_z and *Bi*. For example, if a large particle is used, one can operate at a lower flow-rate and use a longer column to achieve the same Pe_z and *Bi*. This scaling concept is useful for design and economic analysis and will be discussed later.

Overall, increasing interstitial velocity mainly increases the relative importance of intraparticle resistance but has little effect on axial dispersion. Increasing particle size increases both the relative importance of axial dispersion and intraparticle diffusion (Fig. 11). Increasing column length (or L/R ratio) increases Pe_z, N_b, and N_p. However, the longer the column, the smaller the dimensionless pulse size $\Delta\tau$. The effect of $\Delta\tau$ will be discussed later.

Effect of operating and design parameters

Flow-rate. In a chromatographic process, flow-rate is an important operating parameter. It influences resolution, product concentration and cycle time. The question concerning scaling-up chromatographic processes with the proper flow-rate,

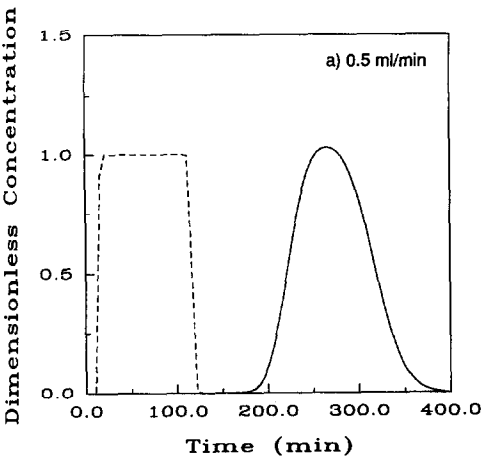

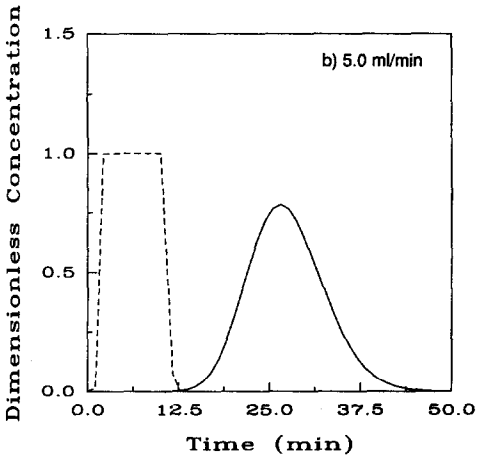

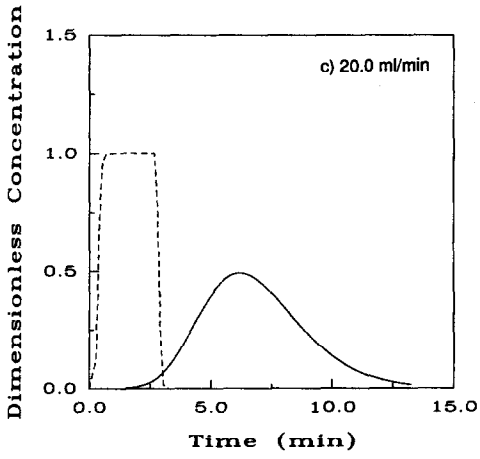

Fig. 12. Replot of effluent histories in real time (min) for the three cases in Fig. 4.

particle size, column length and pulse size will be addressed after the effects of each parameter is discussed.

Fig. 4 shows the simulation results of the lysine–proline system discussed earlier at various flow-rates. An E_p of $4.2 \cdot 10^{-5}$ cm^2/min and $\varepsilon = \theta = 0.45$ were used here. Effluent histories from seven flow-rates ranging from 0.1 ml/min to 40 ml/min are shown here. The pulse volumes are the same for these cases. Little or no change is observed for the proline peak at all flow-rates. This is because proline has a low affinity relative to Na^+. The proline peak passes through the column almost without being retained, and flow-rate has very little effect in this case. The lysine peak becomes broader and its concentration becomes lower as the flow-rate increases. At a flow-rate higher than 20 ml/min, the peak actually becomes asymmetric because of large intraparticle diffusion resistance.

Since the feed pulse concentration of lysine is only 0.01 N, and the α for lysine at this pH is only 1.6, these conditions are close to a linear system where asymmetric peaks are not normally observed. The asymmetry in the lysine peak observed at a flow-rate greater than 20 ml/min is due to mass transfer effect. In order to confirm this, simulations were conducted with a linear isotherm under identical conditions. Asymmetric peaks were also observed. Therefore, the peak asymmetry is largely due to intraparticle diffusion.

The results under the same conditions but with different separation factors are shown in Fig. 7. This case can be viewed as the lysine–proline system at another pH value. Values of $\alpha_{Lys/Na^+} = 4.0$ and $\alpha_{Pro/Na^+} = 0.5$ were used instead. Since both α values are higher, both solutes are retained in the column longer; as a result, both peaks are more spread than before. The effect of flow-rate in this case is similar to that in Fig. 4; as the flow-rate increases, solute band broadens and its concentration decreases. Because of the large α_{Lys/Na^+} value, even at 0.5 ml/min, the lysine peak is already slightly asymmetric. The explanation given for Fig. 1b is also valid here. The tailing of lysine peak at 40 ml/min is due to a combination of intraparticle diffusion resistance and interference effect, because the local equilibrium model also predicts tailing for this peak.

Although increasing flow-rate can decrease the product concentration, it also decreases the elution time, which in turn decreases the cycle time. For certain cases, it may be more economical to speed up the separation process and sacrifice the product concentration. Fig. 12 gives a better representation of the actual time scale involved for the results shown in Fig. 4. Fig. 12a–c are the effluent histories in real time (min) for 0.5, 5 and 20 ml/min, respectively. By increasing the flow-rate from 0.5 to 5 ml/min, the actual cycle time is decreased to about 1/8 of that at the slower flow-rate, whereas the product concentration is only decreased by about 20%.

Particle size. Another way to study the intraparticle diffusion effect is to change the particle size and keep other parameters constant. Increasing the particle size increases Pe_p and Bi, whereas decreases the L/R and Pe_z at the same time. Therefore increasing particle size increases intraparticle diffusion resistance, film resistance, and axial dispersion effects. Fig. 13a flows the simulation results at four different particle radii. These four cases are also represented by circles in Fig. 11. Other parameters are the same as for Fig. 1a.

Increasing particle size decreases product concentrations, and eventually results in asymmetric peaks. As discussed before, the feed pulse concentrations considered

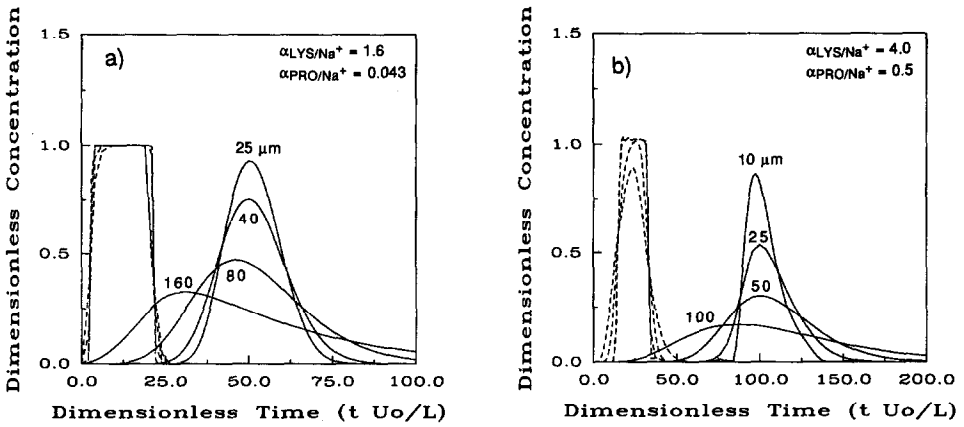

Fig. 13. (a) Effect of particle size. All the other parameters are the same as in Fig. 1a. (b) Effect of particle size at different separation factors. All other parameters are the same as in Fig. 13a.

here are close to those of linear systems. Therefore, the asymmetry of the lysine peak is mostly due to mass transfer effects. For the case at $R = 160\ \mu m$, Bi and Pe_z are 79.6 and 107, respectively. It indicates that intraparticle diffusion is dominating and the effect of axial dispersion is relatively small. Therefore, large intraparticle diffusion resistance can also produce asymmetric peaks.

Although Fig. 13a looks very similar to Fig. 4 in dimensionless time scale, if they were plotted in actual time (t), they would look quite different (see Fig. 12). Each curve in Fig. 4 has a different interstitial velocity (u_0), while all curves in Fig. 13a have the same interstitial velocity. Only a slight decrease in retention time is observed when particle size is increased.

Fig. 13b shows the results of the same system with different solute affinities. The four radii are also represented as circles in Fig. 11. Since $\alpha_{Lys/Na+}$ is 4.0 in this case, asymmetric peaks are observed for particle radius as small as 10 μm. For the proline peak, increasing the particle size does decrease the product concentration in this case, because the $\alpha_{Pro/Na+}$ is larger in this case. As expected, the average retention times for both solutes are longer than in the previous case.

When designing a chromatographic process, it is important to choose the right particle size and flow-rate. This rate equation model provides information on the effects of particle size and flow-rate on resolution and product concentration that local equilibrium models cannot provide. This is a major advantage of using this model for design and scale-up purposes.

Column length. When only the length of the column is increased, and all other parameters are kept constant, Pe_z, N_b and N_p would increase, but $\Delta\tau$ would decrease. In Fig. 14, four column lengths ranging from 1 to 15 cm were considered. For the 15-cm column, good resolution is achieved. However, for this pulse size, the whole column is not fully utilized; also the lysine peak has a lower concentration than the feed. Therefore this case has the problem of long cycle time and low product concentration. When the column is shortened to 7.5 cm, the cycle time is decreased,

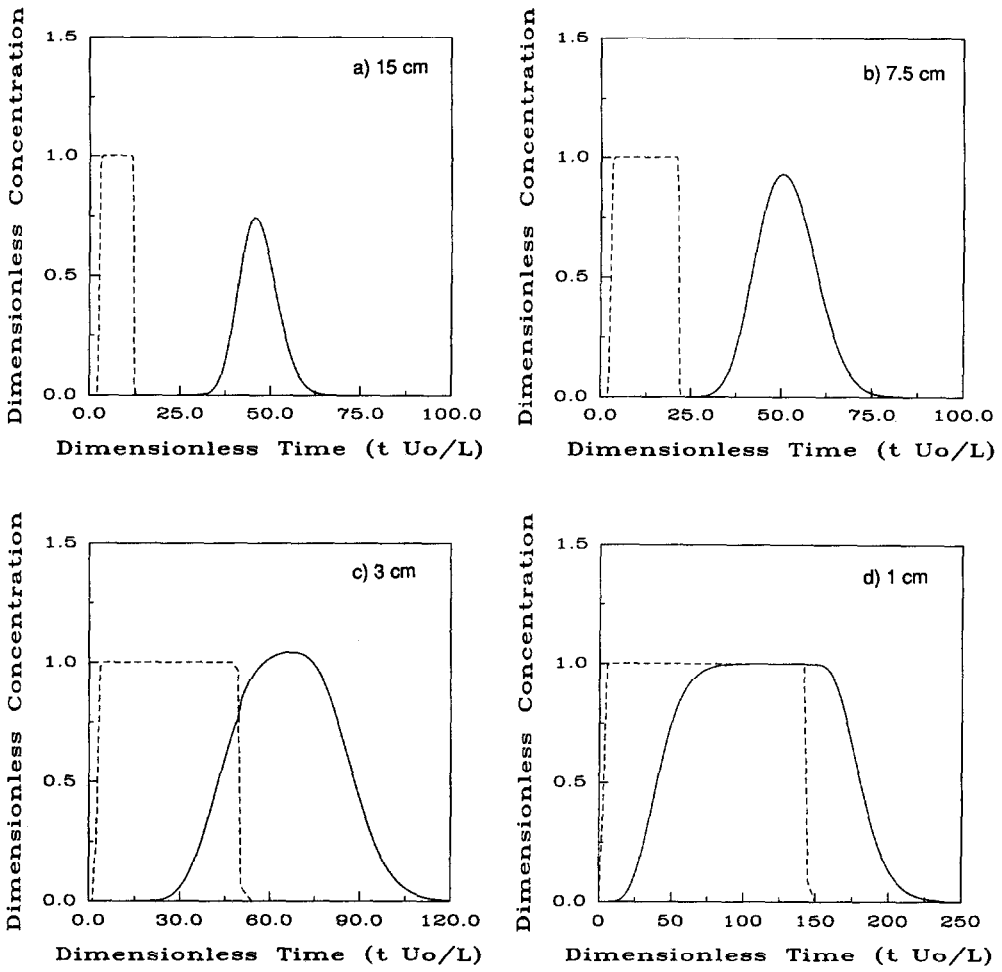

Fig. 14. Effect of column length at $Pe_p = 338$, $Bi = 42$. (a) $L/R = 6000$, $Pe_z = 1340$, $\Delta\tau = 9.43$; (b) $L/R = 3000$, $Pe_z = 670$, $\Delta\tau = 18.86$; (c) $L/R = 1200$, $Pe_z = 223$, $\Delta\tau = 47.15$; (d) $L/R = 400$, $Pe_z = 110$, $\Delta\tau = 141.5$.

and the eluted lysine peak has a higher concentration than for the 15-cm column. This is expected because $\Delta\tau$ is larger for a shorter column.

For the 3-cm column, the two peaks overlap, but part of the lysine peak has a concentration slightly higher than the feed pulse. Therefore, this is another example of trade offs among resolution, cycle time and product concentration. For this case a length between 3 and 7.5 cm would give the best resolution. For the 1-cm column, a large overlap occurs between the two peaks. This column is just too short to resolve the two solutes, even though their separation factors are far apart.

If $\Delta\tau$ is kept constant, a shorter bed has the advantages of a lower pressure drop and a shorter cycle time. If the aforementioned conditions for local equilibrium are met, this is definitely a good strategy. However, in a region far away from local

equilibrium, as L/R decreases, film and intraparticle resistances increase and axial dispersion also becomes more important. As a result, resolution will decrease. In order to achieve the same resolution in a shorter bed, certain scaling rules must be followed, and they will be discussed later.

Pulse size (V_p). Another important operating parameter is the feed pulse size (V_p). An increase in pulse size results in an increase in $\Delta\tau$ and produces similar effects as a decrease in column length. Fig. 15 shows the results of three different pulse sizes in a 7.5-cm column. Very good separation is achieved for the case with a pulse size of 10 ml ($\Delta\tau = 3.77$), but because of mass transfer effects, the concentration of the lysine peak becomes much lower than the feed. When the pulse size is increased to 100 ml ($\Delta\tau = 37.7$), the lysine concentration actually becomes higher than the feed value because of interference, but there is a slight overlap between the two peaks. For the 250-ml case ($\Delta\tau = 94.3$), the pulse volume is 42.4 times the column volume and resolution is poor.

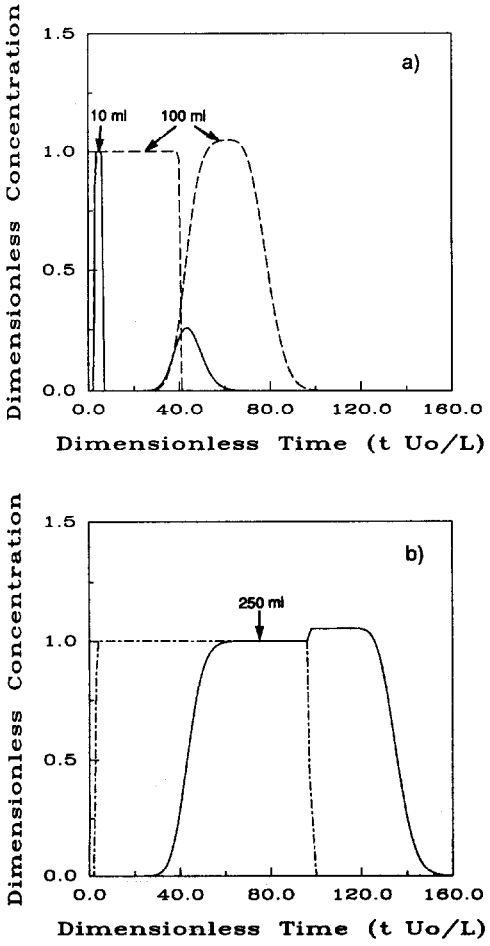

Fig. 15. Effect of pulse size at $Pe_p = 338$, $Bi = 42$, $L/R = 3000$, $Pe_z = 670$. (a) $\Delta\tau$ (10 ml) = 3.77, $\Delta\tau$ (100 ml) = 37.7; (b) $\Delta\tau$ (250 ml) = 94.3.

The effluent history is similar to a smaller pulse with a shorter column, shown in Fig. 14.

Regardless of the differences in pulse volume, solutes in all cases start to elute at about the same times. This is expected for systems with negligible interference effects. Since for a fixed column length and mass transfer resistances, the left flank of the product peak always exits at certain dimensionless time (τ), regardless of its feed pulse volume. Even though the qualitative effects of increasing V_p are similar to decreasing column length, the quantitative results are different because in the latter case, the ratio L/R is also decreased.

Solute concentration. Fig. 16a shows a series of simulations with different solute concentrations in the feed pulse. For all cases both lysine and proline have the same concentration, and the concentration of Na^+ in the feed pulse is 0.18 N; the

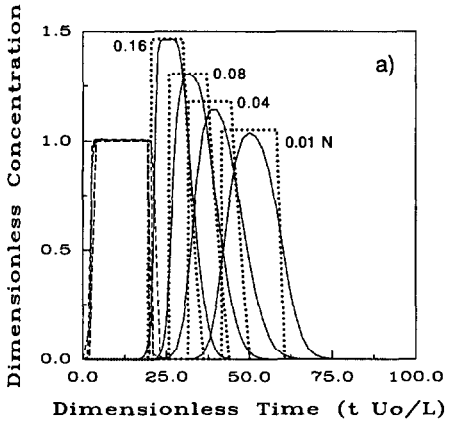

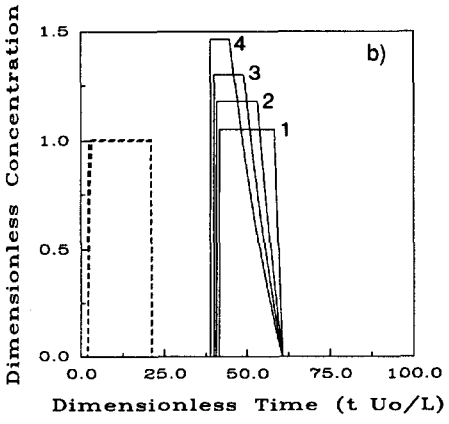

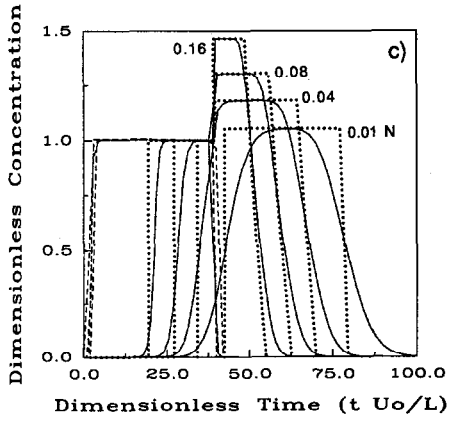

Fig. 16. (a) Effect of solute concentration at $Pe_p = 338$, $Bi = 42$, $Pe_z = 670$, $L/R = 3000$, $\Delta\tau = 18.86$. Lysine histories predicted from the local equilibrium model are shown in dotted lines (····). (b) Effluent histories predicted from the local equilibrium model. The feed fractions of lysine and proline and other parameters are the same as those in Fig. 16a except the total concentration is kept at 0.2 N. Lysine histories are shown in solid lines; proline histories are shown in dashed lines. Concentrations of lysine and proline for 1–4 are listed in Table II. (c) Effect of solute concentration under the same conditions as in Fig. 16a except $\Delta\tau = 37.72$.

concentration of the presaturant and eluent is always equal to the total concentration of solutes plus Na^+ in the feed pulse. All other parameters are kept constant.

As the concentration of proline increases, the eluted proline peak does not change significantly. This is because proline has a much lower affinity relative to lysine and Na^+ and it quickly separates from lysine. As a result, the proline band, despite its high fraction in the feed, is similar to that in a dilute system, in which the feed concentration doesn't affect its product concentration or retention time.

There is, however, a larger change in retention time and effluent concentration for lysine as its feed concentration increases. A higher lysine concentration gives a higher fraction of lysine in the feed as well as a higher total concentration. A higher lysine fraction in the feed results in stronger interference and a higher lysine peak concentration. A higher total concentration results in a shorter retention time. At a feed lysine fraction of 0.235 (0.08 *N*), the lysine peak becomes about 30% more concentrated than the feed. As the feed lysine fraction is increased to 0.32 (0.16 *N*), the lysine peak has a 45% higher concentration than the feed, with only a slight overlap with the proline peak. The results from the local equilibrium model also show more concentrated lysine peaks than the feed. Since the local equilibrium model accounts for only interference effects but not mass transfer effects, it indicates that interference effects dominate in this case. Furthermore, comparison of the predictions from the two models allows us to isolate mass transfer effects from interference effects.

As solute concentration in the feed increases, the significant decrease in lysine retention time is mainly due to the increase in total concentration from 0.2 to 0.5 *N*. This point is verified with the results shown in Fig. 16b, in which the fractions of lysine and proline in the feed are kept the same as in Fig. 16a, whereas the total concentration is kept at 0.2 *N*. The effluent histories predicted from the local equilibrium model are shown. Here the peak lysine concentrations are the same as the corresponding concentrations in Fig. 16a, whereas the retention times are only altered slightly. Comparison of Fig. 16a with Fig. 16b clearly shows the different effects of increasing total concentration from those of increasing solute fraction in the feed.

The results of doubling the pulse size to 100 ml for the system in Fig. 16a are shown in Fig. 16c. The general behavior is similar to that in Fig. 16a. The maximum concentrations of lysine are the same as those in Fig. 16a. This is expected because in the absence of mass transfer effects the maximum peak height due to interference is determined by the lysine fraction in the feed and relative affinities, which are the same in these two figures. However, because of a large pulse size, the lysine and proline peaks overlap for all cases, with the overlap being more severe at higher solute concentrations.

Sodium ion concentration. When the concentrations of the solutes are kept constant and only the concentration of Na^+ in the feed pulse is changed, interference phenomena are observed. The concentration of presaturant and eluent is kept the same as the total concentration of solutes plus Na^+ in the feed pulse. Fig. 17a shows the same lysine–proline system with a 100 ml feed pulse that contains 0.04 *N* each of lysine and proline and various Na^+ concentrations. The fractions of lysine in the feed are 0.333, 0.222 and 0.095 at Na^+ concentrations of 0.04, 0.10 and 0.34 *N*, respectively. The corresponding total concentrations are 0.12, 0.18 and 0.42 *N*. As shown in Fig. 16, the higher the lysine fraction in the feed, the higher the lysine peak concentration in the effluent. Similar results are also seen in Fig. 17a. At an Na^+ concentration of 0.04 *N*,

the lysine fraction in the feed is the highest (0.333). Therefore, the lysine concentration in the effluent is also the highest. However, because the total concentration is the lowest (0.12 *N*), the lysine peak has the longest retention time. In Fig. 16, on the other hand, as lysine concentration in the feed increases, both the lysine fraction and total concentration increase. Therefore, the lysine peak at 0.16 *N* has the highest effluent concentration and the shortest retention time.

Because the three cases shown in Fig. 17a have a large feed pulse ($\Delta\tau = 37.72$) and high solute concentrations, the effluent histories are similar to those predicted from the local equilibrium model. For clarity, only the predicted histories for lysine from the local equilibrium model are shown for comparison; proline histories predicted from the two models are too close to show any difference. This comparison shows that for a concentrated system with a large feed pulse, interference effects control the lysine peak height.

As we reduce the pulse size from 100 to 50 ml ($\Delta\tau = 18.86$) while keeping all other parameters the same, the results are shown in Fig. 17b. The local equilibrium model again predicts the highest lysine concentration in the effluent at $Na^+ = 0.04$ *N*. However, because of a smaller pulse size ($\Delta\tau = 18.86$), mass transfer effects are more pronounced than in Fig. 17a. Furthermore, mass transfer effects are most significant for the lysine peak at $Na^+ = 0.04N$ because the retention time is the longest at the lowest total concentration (0.12 *N*). Because of the significant mass transfer effects, the lysine peak at $Na^+ = 0.04$ *N* has a lower concentration than those at $Na^+ = 0.10$ *N* and 0.34 *N*. For this case, mass transfer effects, not interference effects, control the lysine peak height. The comparison of Fig. 17a with Fig. 17b clearly shows the complexity of interference phenomena coupled with mass transfer effects.

Rate equation model vs. local equilibrium model

Local equilibrium model can generally predict the average breakthrough times of concentration waves, and it usually requires relatively short computation time (a

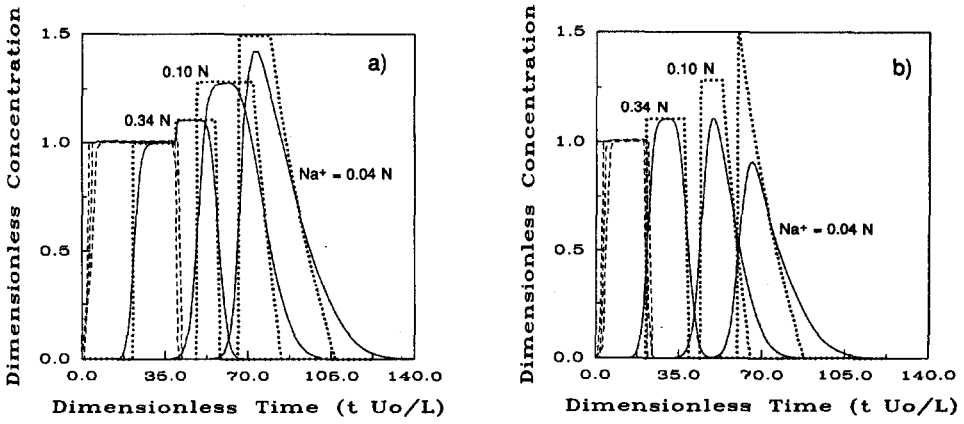

Fig. 17. (a) Effect of sodium ion concentration. The concentration of both lysine and proline is 0.04 *N*; the concentrations of Na^+ are 0.04, 0.10 and 0.34 *N*; $\Delta\tau = 37.72$; other conditions are the same as those for Fig. 16c. (b) Effect of sodium ion concentration under the same conditions as in Fig. 17a except $\Delta\tau = 18.86$.

few minutes on a Gould NP1 computer). It is also a simple model to use for studying interference in complicated operating modes, for example, gradients and two-way flow column operations[8]. It can be used for preliminary design and scale-up purposes when mass transfer effects are insignificant. However, the rate equation model developed here would be a better model to use if (1) mass transfer resistances are important, (2) effects of changing particle size or flow-rate are needed, or (3) isotherms are complex. The only drawback of this model is the long computation time that is required. A two-component elution process typically would take about 1 h on a Gould NP1 computer. The computation time depends on the equilibrium isotherm, the number of collocation points, number of elements used, and how often the elements are updated.

Scaling rules

Finally, we would like to address the question of scaling using dimensionless groups. As shown in our analysis, for a given set of Pe_z, Pe_p, Bi, L/R, $\Delta\tau$, θ, ε, $\bar{C}/C_i$ and feed concentration, this model predicts a unique column profile and effluent history in dimensionless time. As discussed earlier, more than one set of operating and design parameters (F, D, R, L, V_p, E_p, θ and ε) can give an identical set of dimensionless parameters. This means that one can use this model to design and scale up a process for various conditions and scales; as long as the dimensionless parameters are the same, the results in dimensionless variables are identical.

Provided θ, ε and E_p are constant for a given system, the Chung and Wen[13] correlation suggests Pe_z to be a function of L/R and Re. Using the correlation of Wilson and Geankoplis[14] leads to an explicit relation between Pe_p and Bi (eqn. 9). Therefore, only Re, Pe_p, L/R and $\Delta\tau$ have to be kept constant for all other dimensionless parameters to be constant. In order to achieve this, the following three conditions must be satisfied:

$$\frac{FR}{D^2} = \sigma \tag{16a}$$

$$L/R = \beta \tag{16b}$$

$$\frac{V_p}{D^2 L} = \gamma \tag{16c}$$

where σ, β and γ are constants. Eqn. 16a alone is sufficient to keep both Re and Pe_p constant, and eqn. 16c is needed to keep $\Delta\tau$ constant. Thus, we are left with three equations and five variables (F, D, L, R and V_p). Any two variables can be fixed arbitrarily and the other three can be solved from the above equations.

For example, we can consider a standard case: $D = 1$ cm, $R = 25$ μm, $L = 2.5$ cm, $V_p = 50$ ml and $F = 2$ ml/min. This case has the following constants: $\sigma = 5 \cdot 10^{-3}$ ml/(min cm), $\beta = 3000$ and $\gamma = 6.666$. Keeping D the same and scaling R to 2.5 μm would require a 0.75-cm column, 5 ml pulse and 20 ml/min flow-rate. Scaling R to 250 μm, on the other hand, would require a 75-cm column, 500 ml pulse and 0.2 ml/min flow-rate (Table III). All three cases have the same dimensionless parameters, and hence, identical column profiles and effluent history in terms of dimensionless time. However, cycle time, throughput, pressure drop, and amount of packing for these

TABLE III
SCALING USING DIMENSIONLESS GROUPS

	Case 1	*Case 2*	*Case 3*	*Case 4*
D (cm)	1.0	1.0	1.0	10.0
R (μm)	25	2.5	250	2.5
L (cm)	7.5	0.75	75	0.75
F (ml/min)	2	20	0.2	2000
V_p (ml)	50	5	500	500
Relative[a] V_{bed}	1.0	0.1	10	100
Relative cycle time	1.0	0.01	100	0.01
Relative throughput[b]	1.0	10	0.1	1000
Δp[c]	1.0	100	0.01	100
Relative productivity[d]	1.0	100	0.01	100

[a] Relative to the values in case 1.
[b] Throughput $\equiv V_p$/cycle time.
[c] $\Delta P \propto (u_0 L)/R^2$ (Blake–Kozeny equation) 43.
[d] Productivity $\equiv$ throughput/V_{bed}.

three cases are quite different. As shown in Table III, reducing the particle size by ten fold (compare cases 2 and 3 with case 1) can result in a ten-fold reduction in column length, ten-fold increase in flow-rate, and 100-fold reduction in cycle time; it, however, requires a ten-fold reduction in feed pulse and a 100-fold increase in pressure drop. Overall, a ten-fold reduction in particle size can result in a ten-fold increase in throughput (defined here as volume of feed processed per unit cycle time) and a 100-fold increase in productivity (defined here as throughput per unit bed volume).

The throughput for case 2 can be further increased by increasing the column diameter. As shown in case 4 in Table III, a ten-fold increase in diameter can increase the throughput by 100-fold. However, because column volume is also increased 100-fold, the productivity remains the same. The pressure drop for case 4 is the same as for case 2, because column length is kept the same in order to keep L/R constant (eqn. 16b).

In general, the scaling rules of eqn. 16 lead to the following: cycle time is proportional to R^2, throughput is proportional to $1/R$ and D^2, and productivity is proportional to $1/R^2$. Therefore using smaller particles and more rapid cycles can achieve the same resolution but with higher throughputs and higher productivities. Similar conclusions were also reached from a different analysis[23].

CONCLUSIONS

A general rate equation model was used to study the mass transfer effects in isocratic, non-linear elution chromatography. Axial dispersion, intraparticle diffusion, and film mass transfer were considered. This model took into account non-linear isotherms, interference, and size-exclusion effects. Experimental data from ion exchange of amino acids and proteins were in good agreement with the model predictions.

When N_b, N_p and Pe_z become very large, the solution of this rate equation model approaches that of the local equilibrium model. The criteria for approaching local equilibrium conditions depend mainly on α, $\bar{C}/C_i$ and $\Delta\tau$. For example, for $\alpha = 1.6$, $\bar{C}/C_i = 10^3$ and $\Delta\tau = 18.86$, the requirements are $N_b > 4.1 \cdot 10^4$, $N_p > 7.1 \cdot 10^2$ and $Pe_z > 2.7 \cdot 10^3$, whereas for $\alpha = 0.5$ and at the same $\bar{C}/C_i$ and $\Delta\tau$, $N_b > 3.5 \cdot 10^3$, $N_p > 35.6$ and $Pe_z > 670$. For a smaller pulse, $\Delta\tau = 0.377$, a much larger N_b, N_p and Pe_z are required to approach local equilibrium.

The effects of various design and operating parameters on resolution, retention time, peak shape and peak spreading were examined. As flow-rate or particle size increases, Bi increases, which means intraparticle diffusion resistance becomes increasingly more important relative to film resistance. Band spreading due to axial dispersion becomes more pronounced as particle size increases, but it does not increase significantly with increasing flow-rate. Axial dispersion, film diffusion and intraparticle diffusion can all cause peak spreading, peak asymmetry and decrease in retention time. Their effects are more pronounced for systems with small pulses and for solutes with long retention times.

When solute concentration or eluent concentration is increased, retention time is shortened as a result of increasing total concentration. For concentrated feed pulses, interference results in asymmetric peaks and product concentrations which are much higher than their feed concentrations. In general, in the absence of mass transfer effects, the higher the solute fraction in the feed, the higher the solute affinity, the higher the product peak concentration due to interference. However, mass transfer effects tend to reduce peak heights and can have a major influence on the peak concentrations.

Results from a local equilibrium model, which neglects all mass transfer resistances, were compared with those from the rate equation model. The local equilibrium model is easier to use and requires much less computation time, but it can only predict the average breakthrough times of concentration waves. For systems with large pulses and solutes with short retention times, it can give close predictions of dynamics under complicated operating conditions. The rate equation model is much more versatile because it takes into account mass transfer resistances, complex isotherms and size exclusion. However, computation time is much longer. But, if detailed column dynamics are desired for systems with small pulses and solutes of high affinities, the rate equation model should be used.

The dimensionless groups are useful for scaling of nonlinear liquid chromatography. If θ, ε, E_p, $\bar{C}/C_i$ and feed concentration are fixed, as long as Re, L/R and $\Delta\tau$ are kept the same, identical effluent histories in terms of dimensionless variables can be obtained. Applying this scaling rule, one can show that the smaller the particle size, the shorter the cycle time, the higher the throughput and productivity.

SYMBOLS

Bi_j k_jR/E_{pj}, Biot number of the j^{th} component
C mobile phase total concentration based on per bed volume (N)
$\bar{C}$ stationary phase total concentration based on per bed volume (N)
C_i concentration of i in feed on the basis of per bed volume

c_i dimensionless solution phase concentration
c_b dimensionless bulk mobile phase concentration
c_f dimensionless feed concentration
c_p dimensionless solution phase concentration in sorbent particles
c_p^* dimensionless solid phase concentration in sorbent particles
D column diameter
D^∞ Brownian diffusivity (cm^2/min)
E_b axial dispersion coefficient (cm^2/min)
E_p effective diffusivity in the particle phase (cm^2/min)
F flow-rate (ml/min)
J J factor
k mass transfer coefficient (cm/min)
Ke size-exclusion factor
L column length (cm)
n number of species
Pe_z u_0L/E_b, axial Peclet number
Pe_p u_0R/E_p, particle Peclet number
r particle radial axis
R particle radius (cm)
Re $2R\rho u_0\varepsilon/\mu$, Reynolds number
t time (min)
T adjusted dimensionless time, eqn. 14
ΔT dimensionless pulse size, eqn. 13
u_0 interstitial velocity (cm/min)
V_p pulse volume (ml)
V_{bed} column volume (ml)
x dimensionless axial axis
z axial axis (cm)

α_{ij} separation factor of species i against j
ξ dimensionless particle radial axis
$\Delta\tau$ dimensionless time for the pulse
ε void fraction
θ intraparticle porosity
ρ fluid density
μ fluid viscosity
τ dimensionless time ($\tau = tu_0/L$)

ACKNOWLEDGEMENTS

This research was supported by NSF Grants CBT-8412013, CBT-8604906, CBT-8620221 and ECE-8613167. A fellowship from Korea Explosives Company in support of S.U.K. is also acknowledged.

REFERENCES

1 J. J. van Deemter, F. J. Zuiderweg and A. Klinkenberg, *Chem. Eng. Sci.*, 5 (1956) 271.
2 J. C. Giddings, *Dynamics of Chromatography*, Marcel Dekker, New York, 1965.
3 J. A. Jönsson in J. A. Jönsson (Editor), *Chromatographic Theory and Basic Principles (Chromatographic Science Series*, Vol. 38), Marcel Dekker, New York, 1987, p. 27.
4 F. G. Helfferich and G. Klein, *Multicomponent Chromatography Theory of Interference*, Marcel Dekker, New York, 1970.
5 H.-K. Rhee, R. Aris and N. R. Amundson, *Philos. Trans. R. Soc. London, Ser. A*, 267 (1970) 419.
6 H.-K. Rhee and N. R. Amundson, *AIChE J.*, 28 (1982) 423.
7 Q. Yu and N.-H. L. Wang, *Sep. Purif. Methods*, 15 (1986) 127–158.
8 Q. Yu, *Ph.D. Thesis*, Purdue University West Lafayette, IN, 1988.
9 P. Rouchon, M. Schonauer, P. Valentin and G. Guiochon, *Sep. Sci. Technol.*, 22 (1987) 1793–1833.
10 G. Guiochon and S. Ghodbane, *J. Phys. Chem.*, 92 (1988) 3682.
11 D. M. Ruthven, *Principles of Adsorption and Adsorption Processes*, Wiley, New York, 1984.
12 Q. Yu and N.-H. L. Wang, *Comput. Chem. Eng.*, 13 (1989) 915–926.
13 S. F. Chung and C. Y. Wen, *AIChE J.*, 14 (1968) 857.
14 E. J. Wilson and J. Geankoplis, *Ind. Eng. Chem. Fundam.*, 5 (1966) 9–14.
15 J. S. Mackie and P. Meares, *Proc. R. Soc. London, Ser. A*, 232 (1955) 498.
16 F. G. Helfferich, in L. Liberti and F. G. Helfferich (Editors), *Mass Transfer and Kinetics of Ion Exchange (NATO ASI Series E: Applied Sciences*, No. 71), Martinus Nijhoff, The Hague, 1983, p. 162.
17 Q. Yu, J. Yang and N.-H. L. Wang, *React. Polym.*, 6 (1987) 33–44.
18 R. E. Treybal, *Mass-Transfer Operations*, McGraw-Hill, New York, 1980.
19 P. B. Hamilton, D. C. Bogue and R. A. Anderson, *Anal. Chem.*, 32 (1960) 1782.
20 *CRC Handbook of Biochemistry*, CRC Press, Boca Raton, FL, 2nd ed., 1970.
21 P. A. Charlwood, *Biochem. J.*, 57 (1953) 125.
22 N. Wakao and T. Funazkri, *Chem. Eng. Sci.*, 33 (1978) 1375–1384.
23 P. C. Wankat and Y. M. Koo, *AIChE J.*, 34 (1988) 1006–1019.
24 B. H. Arve and A. I. Liapis, *AIChE J.*, 33 (1987) 179.
25 G. Carta and R. L. Pigford, *Chem. Eng. Sci.*, 42 (1986) 511–517.
26 T. L. Chen and J. T. Hsu, *AIChE J.*, 33 (1987) 1387.
27 C. J. Colwell and J. S. Dranoff, *I&EC Fundam.*, 8 (1969) 193.
28 D. D. Do and R. G. Rice, *AIChE J.*, 32 (1986) 149.
29 G. Guiochon, S. Golshan-Shirazi and A. Jaulmes, *Anal. Chem.*, 60 (1988) 1856.
30 E. Kucera, *J. Chromatogr.*, 19 (1965) 237–248.
31 A. I. Liapis and D. W. T. Rippin, *Chem. Eng. Sci.*, 33 (1978) 593–600.
32 C. H. Liaw, J. S. P. Wang, R. A. Greenkorn and K. C. Chao, *AIChE J.*, 25 (1979) 376–382.
33 H. Moon and W. K. Lee, *Chem. Eng. Sci.*, 41 (1986) 1995–2004.
34 M. Morbidelli, G. Storti and S. Carra, *Ind. Eng. Chem. Fundam.*, 21 (1985) 123–131.
35 N. G. Pinto and E. E. Graham, *React. Polym.*, 5 (1985) 49–53.
36 K.-H. Radeke, H.-J. Ortlieb and D. Gelbin, *Chem. Eng. Sci.*, 36 (1981) 11–17.
37 J. B. Rosen, *J. Chem. Phys.*, 20 (1952) 387–394.
38 A. Seidel and D. Gelbin, *Chem. Eng. Sci.*, 41 (1986) 541–548.
39 S.-C. Wang and Chi Tien, *AIChE J.*, 28 (1982) 565–573.
40 T. W. Weber and R. K. Chakravorti, *AIChE J.*, 20 (1974) 228.
41 W. J. Weber and S. Liang, *Environmental Progress*, 2 (1983) 167.
42 Y. W. Wong and J. L. Niedzwiecki, *AIChE Symp. Ser.*, 78 (1982) 120–127.
43 R. B. Bird, W. E. Stewart and E. N. Lightfoot, *Transport Phenomena*, Wiley, New York, 1960.